Detection of small-magnitude Earthquakes using balloon-borne infrasound sensors

Quentin Brissaud 1, Siddharth Krishnamoorthy 2, Jennifer M. Jackson 1, Daniel C. Bowman 3, Attila Komjathy 2 , James A. Cutts 2, Zhongwen Zhan 1, Yan Yang 1, Michael T. Pauken 2, Jacob S. Izraelevitz 2, and Gerald J. Walsh 2

1 Seismological Laboratory, California Institute of Technology, Pasadena, CA; 2 Jet Propulsion Laboratory, California Institute of Technology, Pasadena, CA; 3 Sandia National Laboratories, Albuquerque, NM

1 - INTRODUCTION

Quentin Brissaud narrared the work and can guide you through the poster. Simply play the audio file in each Section. Apologies for the accent.

Fascinating discoveries have recently improved our understanding of Venus from the the observation of current volcanism to the detection of phosphine in its atmosphere. However, the internal structure of Venus remains a mysery as in-situ seismic monitoring is the only viable option to constrain seismic velocities at depth. Yet, due to the harsh temperature and pressure at the surface, monitoring seismic activity through traditional surface sensors is a considerable technical challenge. Taking advantage of the strong seismic-to-acoustic coupling on Venus, a balloon platform floating at 50-60 km above its surface, where temperature and pressure conditions are similar to Earth, seems to be the most promising technique to explore the planet's interior. However, ballon-based seismic monitoring is a new field and the feasibility of detecting natural quakes has not been demonstrated yet on Earth. To address this question, in the weeks following the Ridgecrest sequence in 2019 in Southern California, we flew four balloons on July 22nd and August 9th. By combining the experimental data gathered from ground and balloon-based instruments with high-fidelity seismo-acoustic simulations, we provide a comprehensive picture of quake-induced seismo-acoustic signals as observed from a high-altitude platform. We present a detailed analysis of the dependence of seismic infrasound as measured from a balloon on source parameters, crustal, and atmospheric structure.

2 - THE RIDGECREST BALLOON EXPERIMENT

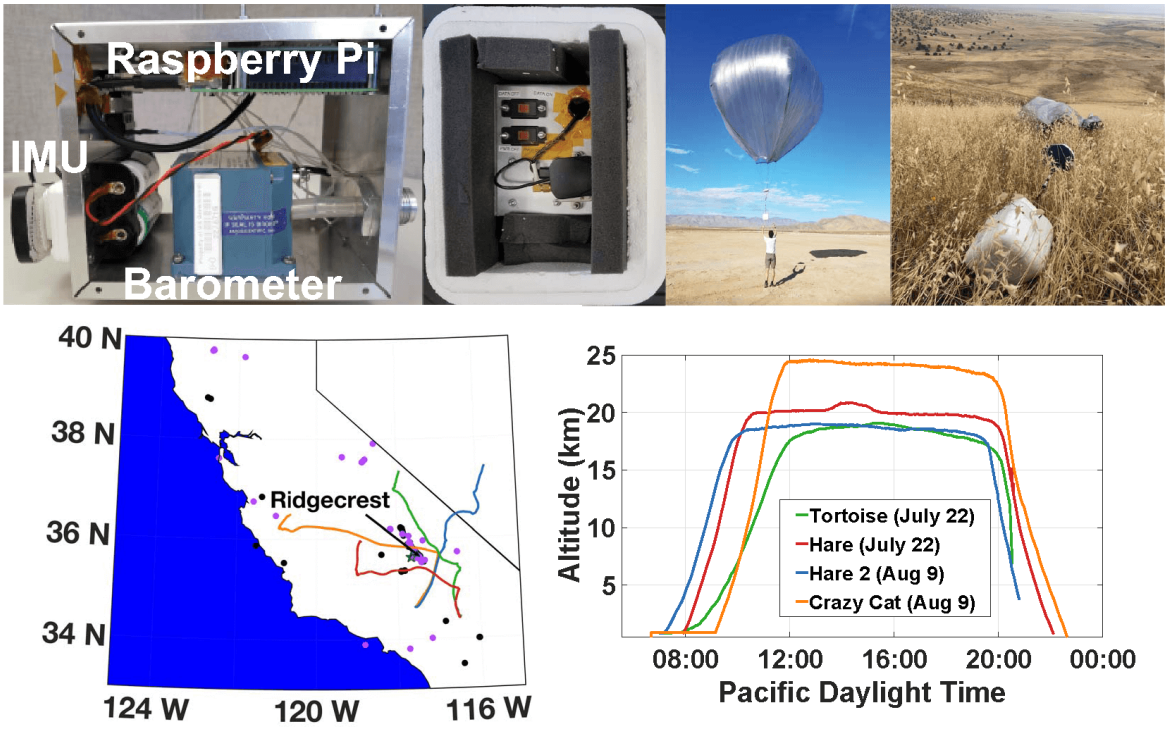

Figure 1: Top row (from left to right): the sensor payload, packaged payload for flight, launching, and recovering the payload. Bottom row (from left to right): the trajectory of the balloons. The Hare and Tortoise balloons flew on July 22, whereas Hare 2 and Crazy Cat balloons flew on August 9. earthquakes with Mw ≥ 1.5 on July 22 are shown as black dots and those on August 9 are shown as magenta dots.

The two large main shocks of the 2019 Ridgecrest earthquake sequence with magnitudes Mw 6.4 and 7.1 occurred on July 4 and July 6, 2019 (10:33 a.m. and 8:19 p.m. local time) respectively. The main shocks induced a lengthy aftershock sequence, which saw the occurrence of over 10,000 earthquakes of Mw 1.5 and above over the next weeks, primarily in the Owens valley region of California (*Ross, 2019*). **As part of a rapid response campaign, we manufactured, tested and launched four "Heliotrope" (*Bowman, 2020*) solar-powered stratospheric balloons equipped with a high-altitude sensor package**. Two of these balloons with a 6~m diameter envelope were launched on July 22, 2019 from Johnson Valley, CA and carried a single sensor package equipped with a Paroscientific Digiquartz 6000-15A-IS barometer and an InertialSense µINS inertial measurement unit (IMU), similar to (*Krishnamoorthy, 2020*).

3 - SEISMIC EVENT SELECTION

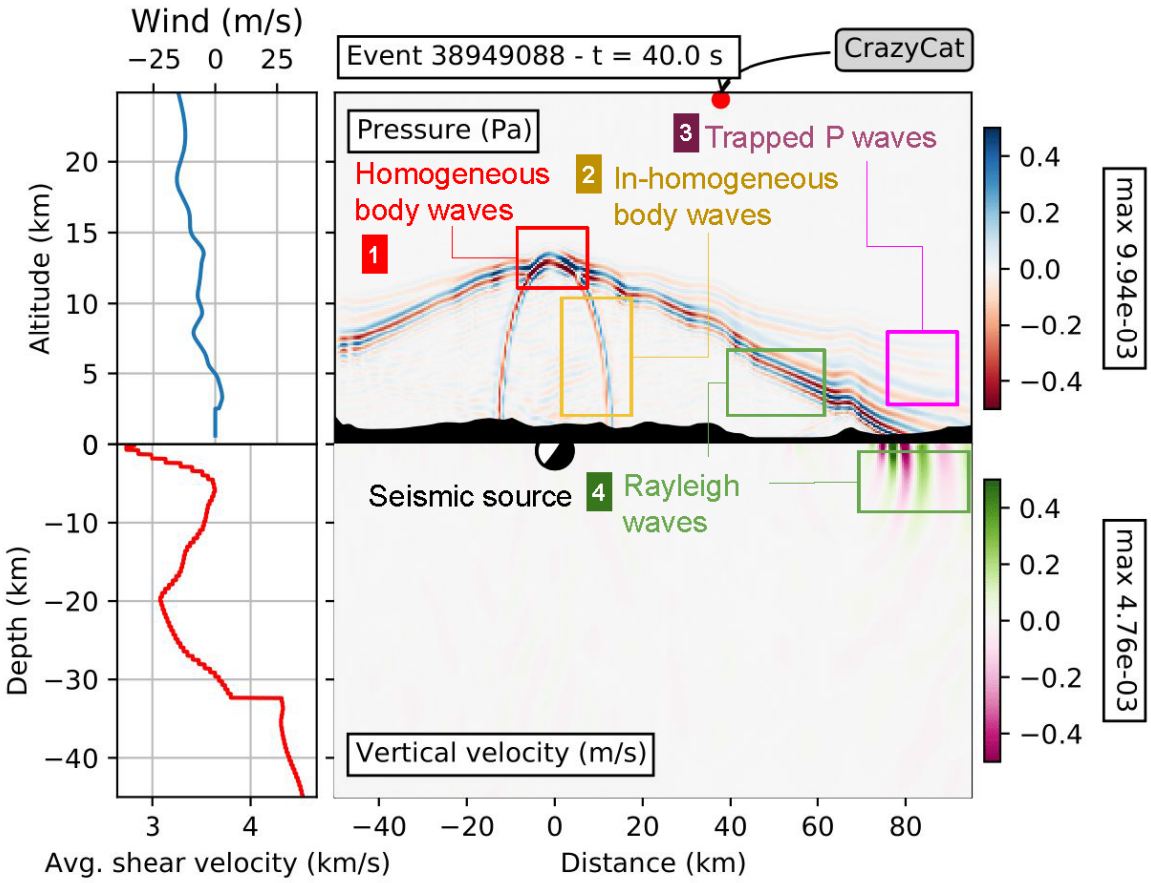

Figure 2: Right, normalized atmospheric pressure and seismic vertical-velocity wavefields against epicentral distance (km) and altitude or depth (km) at t = 40 s after event E2c - 38949088 on August 9th. Topography is shown as a black surface in the top panel. The beachball represents the focal mechanism and indicates the source location.

The acoustic wavefield in the atmosphere excited by an earthquake includes both epicentral and Rayleigh-wave induced infrasound phases (see Figure 2). To prioritize the seismic events and narrow down the investigation of pressure signals we adopt a four-steps procedure:

1. we **predict the arrival times of epicentral infrasound for each event along the balloon path using the ray tracing software GeoAc** (*Blom, 2012*) and prioritize events with the closest ray paths to the balloon paths in terms of both time (< 2s) and space errors (< 2km)
2. we **predict the Rayleigh-wave-induced acoustic wave amplitudes for each event using a semi-analytical modeling tool, RW-atmos**, developed for this study, and prioritize events in terms of pressure amplitudes. We neglect events with predicted amplitudes p < nl/25, where nl is the average noise level in the 1-5Hz frequency band, to account for site effects. RW-atmos allows for the fast computation of 3d pressure wavefields excited by Rayleigh waves in the source's far-field. RW-atmos first resolves Rayleigh-wave Green's functions in 3d using 1d seismic models to provide an initial vertical-velocity forcing wavefield. Time-dependent vertical motions are then propagated in the atmosphere in the frequency-wavenumber domain by solving the acoustic dispersion equations considering a stratified atmosphere with homogeneous layers
3. we **update predicted pressure amplitude by accounting for local site effects using seismic records at the surface**. The scaling factor is computed as the ratio between the maximum recorded seismic amplitudes and the maximym predicted seismic amplitudes
4. we perform a visual inspection of each scalogram computed from the recorded pressure and seismic data to detect any potential arrival. When an arrival is detected, we **compute the cross correlations between seismic and acoustic data and simulated waveforms to assess the causality between seismic and acoustic phases**.

4 - EPICENTRAL AND RAYLEIGH-WAVE INFRASOUND

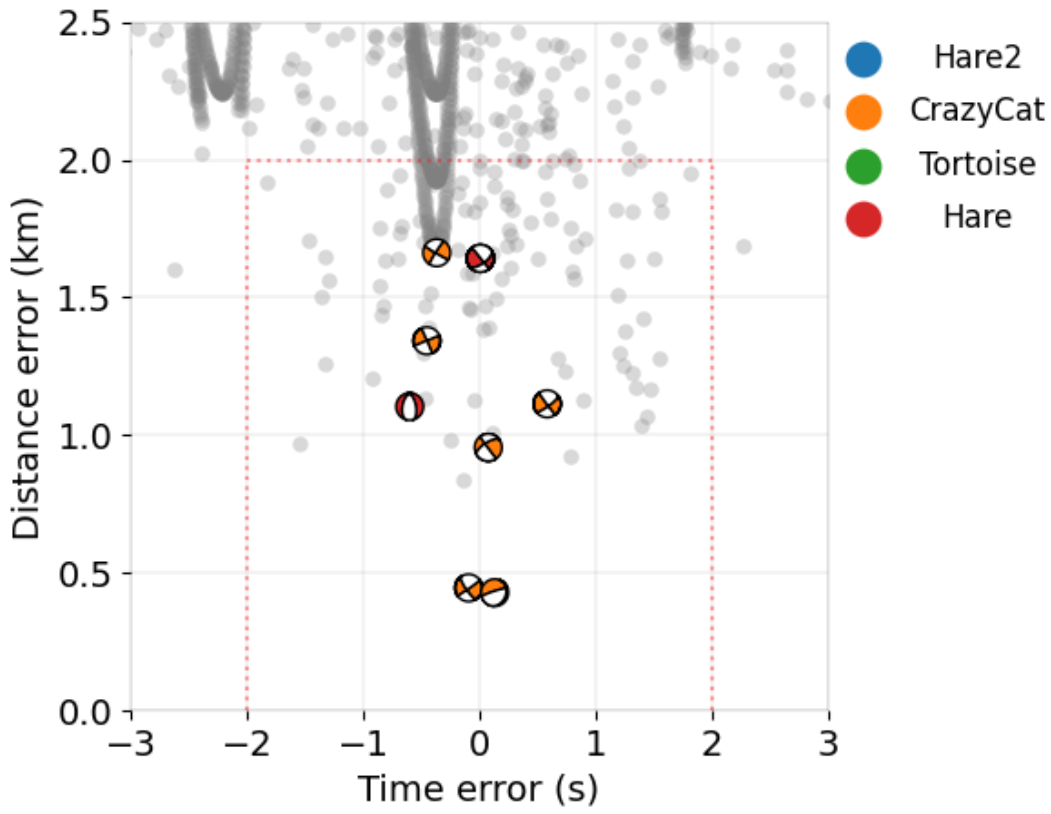

Figure 3: Ray tracing results for epicentral infrasound. Distance error (km) against time error (s) between ray paths crossing the balloon path within a radius a 2 km for the seismic events in the SCSN catalog on July 22nd and August 9th at the balloons. The grey background dots correspond to all the ray locations (i.e. all the rays and all their path) that fulfill the time-distance "detection" conditions. We highlight the best solutions for each ray with beachball representing the associated focal mechanism.

We found only few possible epicentral infrasound detections at the balloons (see Figure 3). Balloons were located in the acoustic shadow zone (*Thompson, 1972*) for most events which explains the lack of clear arrival of infrasound generated by seismic body waves. Additionally, because low-magnitude events generate high-frequency seismic waves > 1Hz, events on July 22nd and August 9th were too deep for in-homogeneous seismic waves to efficiently couple with the atmosphere and excite atmospheric waves isotropically above the source (*Godin, 2011*).

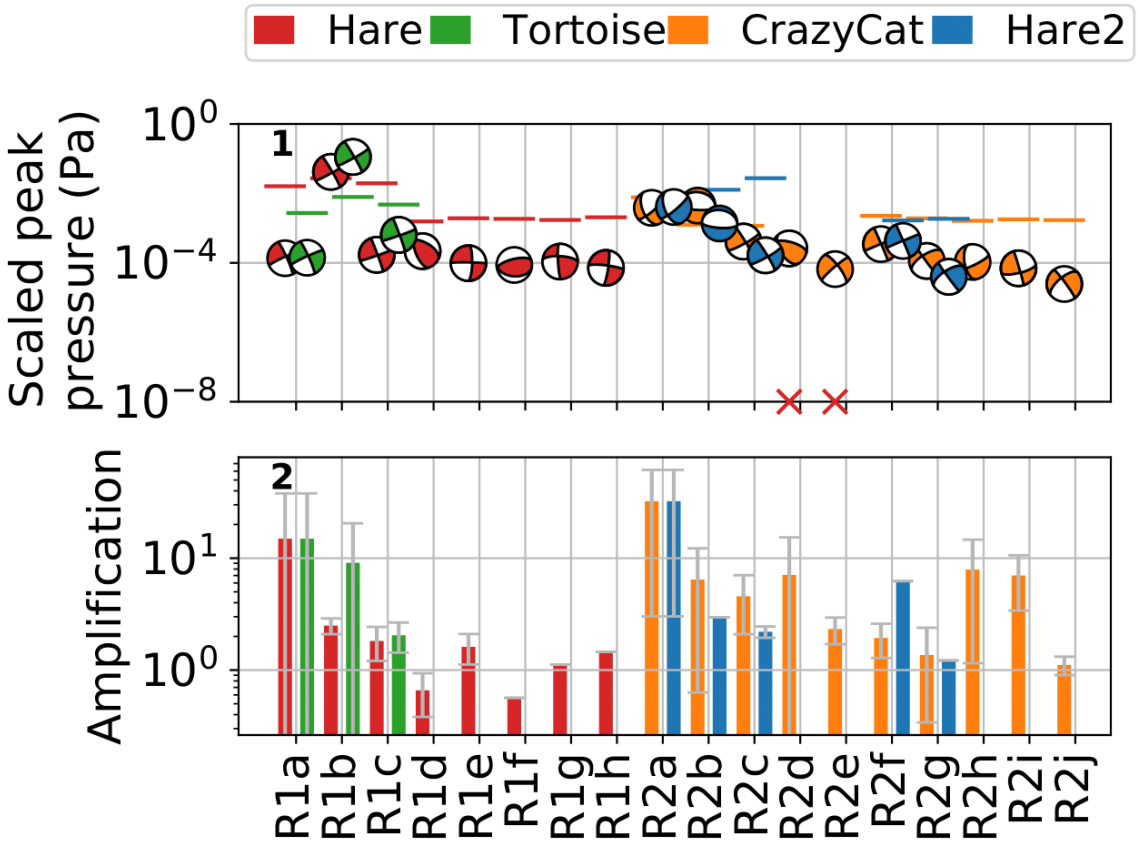

Figure 4: Semi analytical results for Rayleigh-wave infrasound. 1) simulated peak pressure (Pa) at the balloon for each selected event, presented in Table 1, multiplied by the amplification factor, i.e. peak vertical velocity ratio between seismic data over simulated signals, presented in 2). Peak amplitudes are represented by the beachballs of each focal mechanism with colors corresponding to each balloon. Horizontal lines correspond to the noise level. Red crosses indicate events for which the signal is polluted by large-amplitude spurious noise. The amplification is given as an average from the closest regional seismic stations. The corresponding standard deviation is shown as grey error bars around each bar.

While most events show low signal-to-noise ratios, i.e. scaled predicted pressure below the noise level, **our model predicted a strong arrival for our largest event (Figure 4), a moment-magnitude 4.2 earthquake referred as R1b**, during the ascending phase of both Tortoise and Hare.

5 - A POSSIBLE DETECTION?

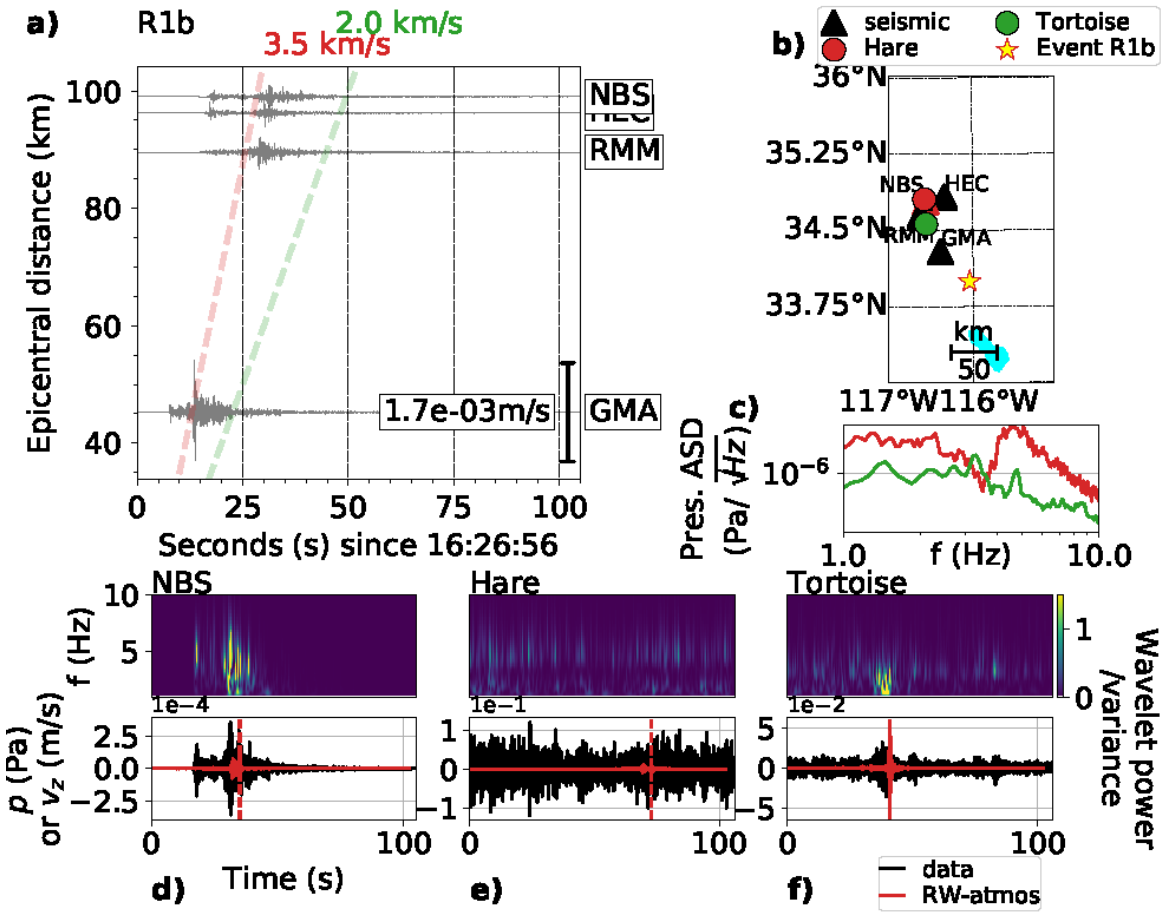

Figure 5: Seismo-acoustic data for event R1b - 38624279. a), seismic vertical-velocity (m/s) timeseries for event 38624623 against epicentral distance (km). b), location of seismic stations and balloons at the time of event. c), background pressure noise levels (Pa/√ Hz) as experienced by Hare and Tortoise barometers. d), seismic scalograms normalized by variance and corresponding timeseries for the closest seismic stations to the balloons from the data (black) and the RW-atmos simulations (green). e) and d), pressure scalograms normalized by variance for the available balloons at the time of the event from the data (black) and the RW-atmos simulations (green). The dashed vertical green line corresponds to the time of simulated timeseries maximum.

Semi-analytical results (see Figure 5) indicate a strong arrival at both Tortoise and Hare on July 22nd at 32s after event R1b. To further investigate this arrival at Tortoise, we ran a full-waveform simulation of the coupled seismo-acoustic waves including topography and attenuation for event R1b (see Figure 6).

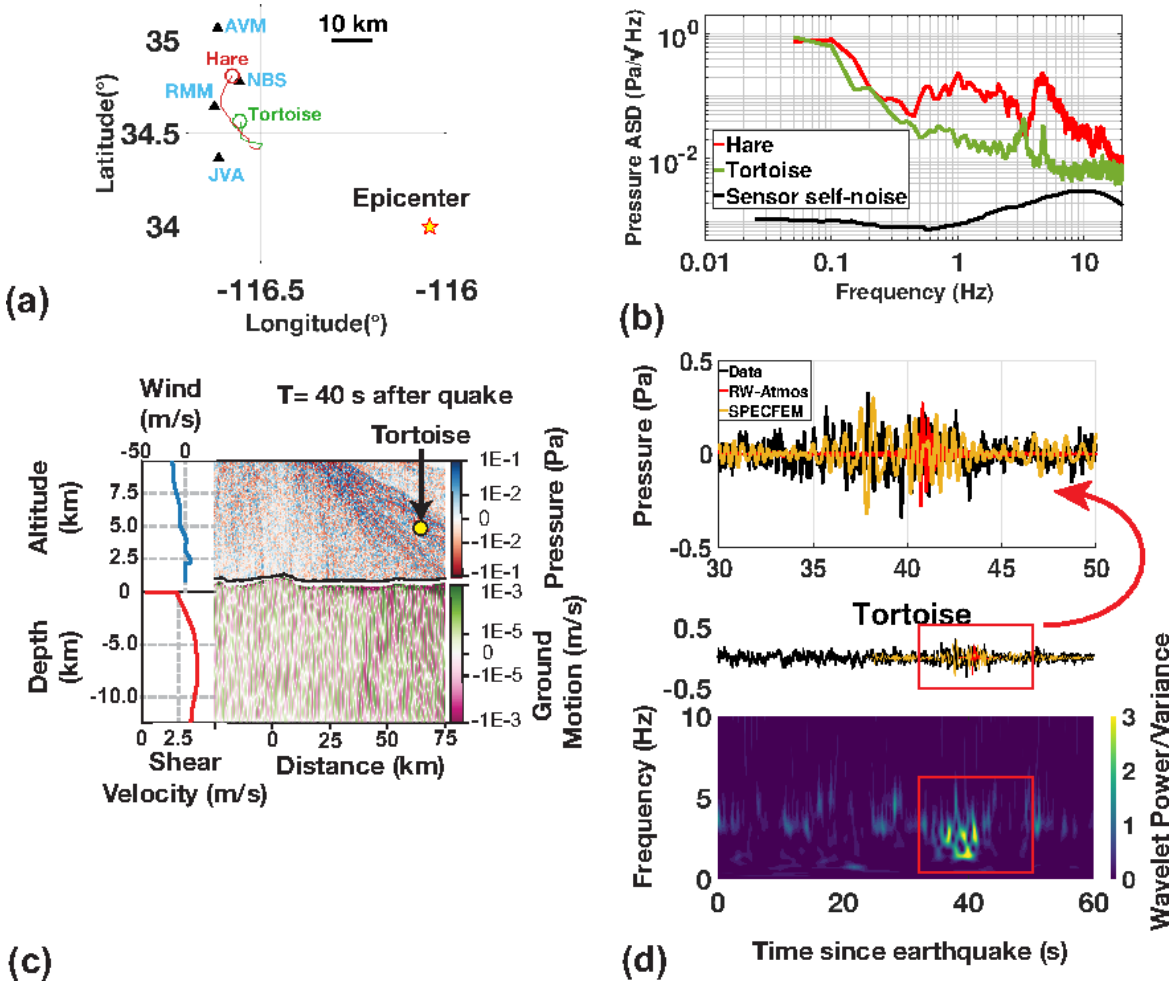

Figure 6: (a) The relative location of the balloons (circles), ground-based seismometers (triangles) and the epicenter (star), (b) Background pressure noise levels as experienced by Hare and Tortoise barometers – Hare was rising through the atmosphere at a faster speed and experiences a greater noise background, especially in the 1-10 Hz band, where the signal appears. Peaks at >3 Hz in the frequency spectrum are caused by vortex shedding from the envelope. The black line represents the sensor electronic self-noise level, (c) A snapshot of the SPECFEM2D-DG simulation showing the propagation of the seismic wave along the Earth's crust and the arrival of the infrasound signal at Tortoise, (d) Time-series as recorded by the Tortoise barometers compared with RW-Atmos and SPECFEM2D-DG simulation tools, with the inset magnified to show agreement between simulated and recorded data. Simulated waveforms were first scaled down by a factor of 4000 to account for geometerical spreading, then scaled up by a factor of 4.77 after comparison with ground motion data from the nearest seismometer (RMM) to compensate for local site effects

A clear quasi-planar acoustic wavetrain is visible traveling through Tortoise and corresponding to the arrival observed in the pressure records in Figure 6 b). Simulated pressure timeseries at Tortoise show consistent amplitude and arrival time with the pressure data at Tortoise for the first Rayleigh-wave packet at 40s in the 1-3Hz frequency range. The second wave packet arriving around 50s in our simulations is less visible in the acoustic data at Tortoise. We hypothesize that the absence of this arrival owes to large near-surface attenuations that have a strongest impact on the fundamental mode is more than on the higher-order modes (*Aki and Richards, 2002, Ch.7*). Unfortunately, signals recorded at Hare were polluted by high-frequency spurious noise generated by vortex shedding during the rapid balloon ascension (*Krishnamoorthy, 2020*).

6 - DISCUSSION

Manuscript will be submitted soon. Do not hesitate to contact quentin@norsar.no to get updated when the preprint/publication will be available.

We investigated the seismo-acoustic wavefield excited by the small-magnitude earthquakes in Southern California. We proposed a simple four-steps procedure to investigate large datasets of seismo-acoustic observations for a small computational cost. **One strike-slip event of magnitude 4.2 event produced large-enough surface waves to be theoretically detected at 4.8km altitude, 78km from the epicenter**. Comparisons between the pressure data and full-waveform numerical simulation seem to indicate a possible seismically-induced acoustic arrival. The acoustic signal is characterized by a narrow-band energy peak (1-3Hz) and could correspond to a higher-mode Rayleigh wave.

However, **because most events are dominated by high frequencies and a strong strike-slip component, epicentral and Rayleigh-wave-induced infrasound are generally characterized by low signal-to-noise ratio << 2**. Most refracted epicentral waves do not reach the sensors as the balloons generally remain in the acoustic shadow zone at regional distances. Furthermore, events were too deep for the low-frequency acoustic energy to propagate isotropically from the source (*Averbuch, 2020*). In the far field, the presence of topography led to both a strong Rayleigh-wave wave scattering for large topographic gradients at high frequency (*Wang, 2015*) and defocusing in the atmosphere at low frequency drastically reducing the acoustic amplitudes at the balloon. Finally, the significant environmental and instrumental noise levels, explained by both the large vortex shedding >3Hz generated by the upward motion of the balloon and the limited number of sensor on each balloon, prevented high-frequency observations. A straightforward mitigation strategy to increase the signal-to-noise ratio would consist in adding extra sensors to discriminate between travelling and spurious waves (*Krishnamoorthy, 2020*).

However, **all these observations apply primarily to high-frequency shallow earthquakes with significant seismic energy trapped in sedimentary layers**. On Venus, quakes up to magnitude 6 have been hypothesized to trigger at the bottom of the seismogenic layer (*Garcia, 2005*). Therefore, the low-frequency energy generated by such large magnitude quakes will be less sensitive to small-scale variations of topography and seismic velocities in the near surface.

DISCLOSURES

AUTHOR INFORMATION

Quentin Brissaud, Research Scientist at NORSAR (quentin@norsar.no; twitter @QuentinBrissaud)

ABSTRACT

The mechanical coupling between a planet and its atmosphere enables the conversion of seismic waves into infrasound waves, i.e. low-frequency pressure perturbations (< 20Hz), which propagate to the upper atmosphere. Since the characteristics of the seismically-induced pressure perturbations are connected to their seismic counterparts, they provide a unique opportunity to investigate the atmospheric and interior structures of a planet or to constrain source properties. However, in Earth's remote regions, deploying seismic or infrasound networks at the surface can be a difficult task. Stratospheric balloon platforms equipped with pressure sensors have therefore gained interest since they provide a unique and inexpensive way to record pressure signals in the atmosphere with a low noise level. Yet, infrasound observations of Earthquakes on balloon platforms have never been reported in the literature. In this study, we investigate the seismo-acoustic wavefield generated by the aftershocks of the 2019 Ridgecrest sequence and other regional low-magnitude Earthquakes on July 22 and August 9, 2019 using four free-flying balloons equipped with pressure sensors. We observed a strong signal coherence after the largest event between seismic motions at the surface and balloon pressure variations which matches our numerical simulations. A first atmospheric earthquake detection is crucial to demonstrate the viability of this novel technique to monitor infrasound from natural and artificial seismicity on Earth, and the study of seismic activity on planets such as Venus.

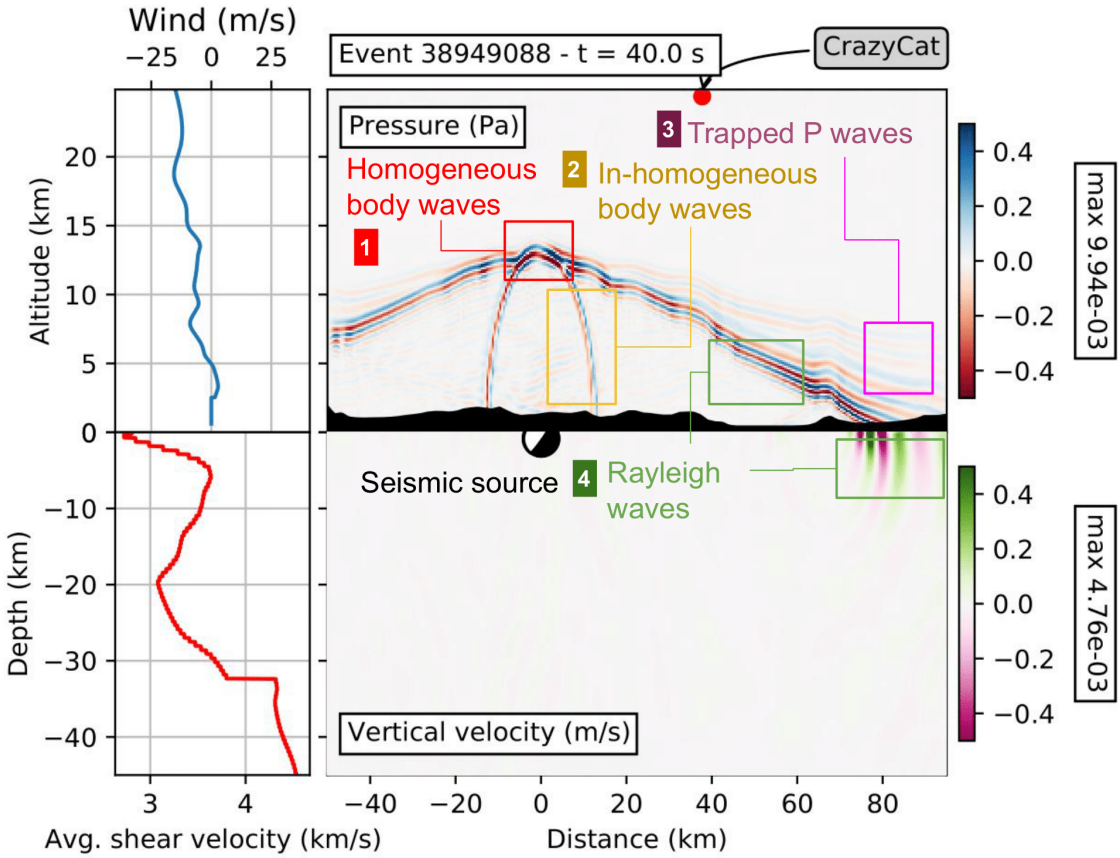

(https://agu.confex.com/data/abstract/agu/fm20/8/3/Paper_674838_abstract_644917_0.png)

REFERENCES

Aki, K. and Richards, P. (2002).Quantitative Seismology. University Science Books.

Averbuch, G., Waxler, R. M., Smets, P. S., and Evers, L. G. (2020). Probabilistic inversion for submergedsource depth and strength from infrasound observations.The Journal of the Acoustical Society of America,147(2):1066–1077.

Blom, P. and Waxler, R. (2012). Impulse propagation in the nocturnal boundary layer: Analysis of thegeometric component.The Journal of the Acoustical Society of America, 131(5):3680–3690.

Bowman, D. C., Norman, P. E., Pauken, M. T., Albert, S. A., Dexheimer, D., Yang, X., Krishnamoorthy, S.,Komjathy, A., and Cutts, J. A. (2020). Multihour Stratospheric Flights with the Heliotrope Solar Hot-AirBalloon.Journal of Atmospheric and Oceanic Technology, 37(6):1051–1066.

Garcia, R., Lognonn´e, P., and Bonnin, X. (2005). Detecting atmospheric perturbations produced by Venusquakes.Geophysical Research Letters, 32(16).

Godin, O. A. (2011). Low-frequency sound transmission through a gas–solid interface.The Journal of theAcoustical Society of America, 129(2):EL45–EL51

Krishnamoorthy, S., Bowman, D. C., Komjathy, A., Pauken, M. T., and Cutts, J. A. (2020). Origin andmitigation of wind noise on balloon-borne infrasound microbarometers.The Journal of the AcousticalSociety of America, 148(4):2361–2370.

Thompson, R. J. (1972). Ray theory for an inhomogeneous moving medium.The Journal of the AcousticalSociety of America, 51(5B):1675–1682.

Wang, L., Xu, Y., Xia, J., and Luo, Y. (2015). Effect of near-surface topography on high-frequency rayleigh-wave propagation.Journal of Applied Geophysics, 116:93–103.